Research Article | Vol. 16, No. 11 / 1 Nov 2025 / Biomedical Optics Express 4392

Biomedical Optics EXPRESS

Keratoconus diagnosis based on macro-micro corneal characteristics via optical coherence tomography

CHANGYONG CHEN,[1,†] FAN ZHANG,[2,†] YUN TANG,[1,†] HUIDOU CAO,[1] LINGMEI CHEN,[1] SHUHAO QIAN,[1] LU YANG,[1] JIA MENG,[1] RUSHAN JIANG,[1] CHUNCHENG WANG,[1] SHUANGMU ZHUO,[3] ZHIHUA DING,[1] MEIXIAO SHEN,[2] ZHANGLIANG LI,[2] FANGJUN BAO,[2,5] YUN-E ZHAO,[2,6] AND ZHIYI LIU[1,4,*]

[1] *State Key Laboratory of Extreme Photonics and Instrumentation, College of Optical Science and Engineering, International Research Center for Advanced Photonics, Zhejiang University, Hangzhou, Zhejiang 310027, China*
[2] *State Key Laboratory of Eye Health, Eye Hospital, Wenzhou Medical University, Wenzhou 325027, China*
[3] *School of Science, Jimei University, Xiamen, Fujian 361021, China*
[4] *Jiaxing Key Laboratory of Photonic Sensing & Intelligent Imaging, Jiaxing, Zhejiang 314000, China*
[5] *baofjmd@wmu.edu.cn*
[6] *zye@eye.ac.cn*
[†] These authors contributed equally.
[*] *liuzhiyi07@zju.edu.cn*

Abstract: Keratoconus is an ophthalmopathy characterized by a central thinning that commonly causes irregular astigmatism and high myopia. However, the diagnostic standards of keratoconus have not yet been well established clinically and mainly rely on macro characteristics measured through corneal topography. To describe the micro changes conveyed by collagen microstructures in the corneal stroma and provide a new insight for keratoconus, we developed a quantitative diagnostic method combining macro-micro information via *in vivo* optical coherence tomography (OCT). A comparison experiment was designed to confirm the feasibility of characterizing collagen organization using OCT. Macro variables, including heterogeneity in curvature and thickness of cornea, and micro variables of collagen fiber alignment, were calculated and weighted to define the keratoconus potential index (KPI) as a quantitative measure for diagnosing keratoconus and mapping disease risks of 104 participants, which showed excellent diagnostic power (with an area under the curve of 0.991) in keratoconus detection.

1. Introduction

Keratoconus is an ophthalmopathy characterized by a central thinning with a conical protrusion, which causes irregular astigmatism and high myopia [1,2]. Despite the high prevalence of the disease, its etiology is still complicated. Studies in the fields of genetics and small molecule bioanalysis indicate that the disease may be multifactorial in origin [3]. In the early stages of keratoconus, there may only be a rapid increase in myopia and astigmatism with few specific symptoms [4], which makes it difficult for most patients to notice the situation in time. Corneal topography is the main reference for diagnosing corneal keratoconus today by examining the entire corneal surface morphology to detect changes such as abnormal elevation of the typical anterior surface of the cornea [5,6]. In addition, corneal biomechanical examination demonstrates decreased biomechanical indices such as corneal hysteresis and resistance factor [7–9], and corneal thickness examination reveals features such as central thinning [9,10]. At present, the diagnostic standards and treatment modalities of keratoconus are still inconsistent and

#576715 https://doi.org/10.1364/BOE.576715
Journal © 2025 Received 19 Aug 2025; revised 30 Sep 2025; accepted 7 Oct 2025; published 10 Oct 2025

Biomedical Optics EXPRESS

controversial [11], while most physicians can only rely on their personal experience in the clinical diagnosis because of the lack of quantitative standards [12].

Optical coherence tomography (OCT) is an optical imaging technique based on the principle of the weakly coherent light interference, which can obtain two-dimensional (2D) or three-dimensional (3D) structural images of biological organisms at different depths [13,14]. OCT has been widely applied in ophthalmic examinations due to its advantages in providing *in vivo*, non-contact, high-axial-resolution tomographic imaging for ocular tissues [15–17]. The applications of OCT in keratoconus diagnosis have been well explored. For example, OCT can be used to map corneal epithelial thickness and derive related variables for keratoconus evaluation [18,19]. High-resolution Fourier-domain OCT has shown good repeatability of corneal epithelial thickness measurements in both normal and disease groups [18]. These findings may provide useful insights through changes in corneal thickness over time in situations where the topography is uncertain. In addition, the use of swept source optical coherence tomography (SS-OCT) allows measuring parameters such as posterior and anterior height, optic thickness, corneal density and generating corneal elevation maps, which can be used to differentiate between keratoconus and normal corneas [20]. However, previous studies focused on the characteristics of macrostructural changes for qualitative analysis mainly, which may be challenging to achieve high sensitivity and specificity in keratoconus diagnosis, and external deformations often indicate that the situation has been advanced with the best treatment period missed [11,21]. Although OCT is useful in measuring corneal and epithelial thickness, variations associated with the keratoconus process are complicated. Especially, microscopic features of collagen structures, one of the main components within the cornea, are suggested to alter with initiation and progress of keratoconus [22]. Therefore, it might be inadequate to sustain the diagnosis of keratoconus with macroscopic features only.

In this study, we developed a macro-micro combined method based on OCT images to understand and diagnose keratoconus. Specifically, we selected two typical macroscopic variables including heterogeneity in corneal curvature and thickness to describe the external corneal deformation. In particular, at the microscopic level, we characterized the changes of collagen fiber alignment during the progression of corneal lesions. Afterwards, we evaluated the importance of the three variables to derive the keratoconus potential index (KPI) as a unified and clinician-friendly parameter and assessed its performance in mapping and diagnosis of keratoconus.

2. Materials and methods

2.1. Participants

OCT imaging was done clinically at the Eye Hospital of Wenzhou Medical University, with written informed consent obtained from all participants. In total 104 participants were involved in this study, with 51 patients diagnosed as keratoconus, and the other ones being normal controls. The inclusion criteria of normal group required bilateral normal corneal findings on comprehensive eye examination, including ordinary slit-lamp biomicroscopy, corrected distance visual acuity of 20/20 or better, normal topographic patterns, and absence of ocular surgery or trauma history. For the keratoconus groups, participants needed to demonstrate characteristic topographic distortions, such as skewed asymmetric bow-tie patterns or inferior steepening, and accompanied by at least one clinical sign of keratoconus, including but not limited to Munson's sign, Vogt's striae, Fleischer's ring, apical thinning, or Rizzuti sign [23]. The normal and keratoconus eyes were photographed along the arc-sagittal direction [Fig. 1(a)], using a commercial OCT (RTVUE XR, OPTOVUE, USA). For each patient, one eye was designated as the study eye; if both eyes were eligible for inclusion, the eye with the worse keratoconus at screening was selected. The optical axial and lateral resolutions of the system were 5 μm and 15 μm, respectively, and the axial imaging depth was 2 mm. The field of vision range was

Biomedical Optics EXPRESS

12×9 mm ($x \times y$) containing 1536×640 pixels, and the total acquisition time for each field of view was about 3 s.

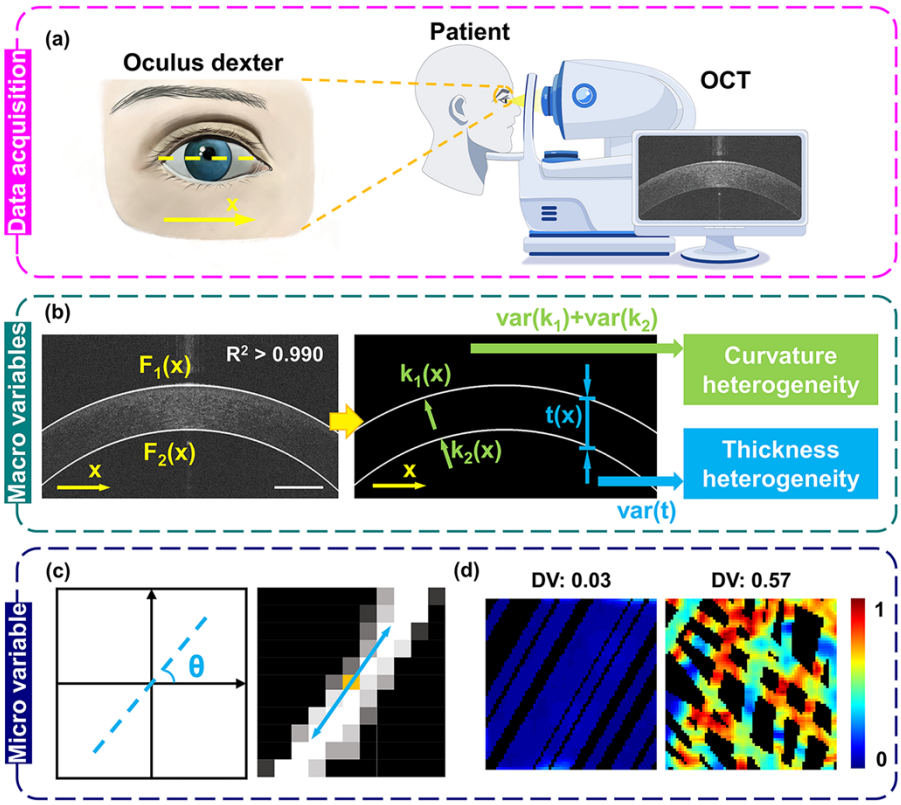

Fig. 1. Data acquisition and quantitative analysis methods. (a) Schematic of *in vivo* human corneal OCT images acquisition at the hospital. Images were acquired in the more advanced eye near the equator along the arc-sagittal direction (yellow dashed line). (b) Macro variables calculation method. The upper and lower boundaries trajectory functions were fitted, with R^2 marked. The curvature distribution function k(x) and the thickness distribution function t(x) were derived based on the boundary trajectory, respectively. The sum of the variance in curvature from upper and lower boundaries was taken as the curvature heterogeneity, and the thickness variance among different x locations was taken as the thickness heterogeneity. Scale bar, 1.5 mm. (c) Micro variable calculation method. The orientation angle θ was defined (left), calculated from the weighted vector summation method (right). (d) Simulated fiber stacks with high (left) and low (right) alignment were used to test the directional variance (DV) metric, defined as the micro variable to describe the collagen fiber disorder with values marked on top of maps.

2.2. *Macro variables calculation method*

The upper and lower corneal boundaries were extracted using the fitted boundary method (Supplement 1, Fig. S1). Specifically, we manually selected the corneal upper and lower boundary sampling points and obtained the fitted functions $F_1(x)$ and $F_2(x)$ [marked in Fig. 1(b)] based on high-order polynomial. The goodness of fit defined as coefficient of determination R^2 for all samples was above 0.990, indicating that the fitting function provided excellent agreement to the corneal boundaries (Supplement 1, Fig. S2). After this, the curvature distributions of the upper and lower boundaries could be calculated separately (Supplement 1, Fig. S3), based on the

Biomedical Optics EXPRESS

curvature calculation formula as:

$$k(x) = |f''(x)|/(1 + f'(x)^2)^{3/2}, \tag{1}$$

where $F(x)$ included the upper and lower boundary functions, while $f''(x)$ and $f'(x)$ were its second-order and first-order derivatives. $k(x)$ included $k_1(x)$ and $k_2(x)$ [pointed by green arrows in Fig. 1(b)].

After calculating the curvature for all samples, we assigned an empirical value of 16 as the maximum to normalize the curvature at each point. The curvature heterogeneity (CH) was defined as the sum in variance of the normalized curvature from upper and lower boundaries [Fig. 1(b)]:

$$CH = \mathrm{var}(k_1) + \mathrm{var}(k_2). \tag{2}$$

Based on the upper and lower boundary functions, it was easy to obtain the thickness of the cornea at each pixel along the x-direction [pointed by blue arrows in Fig. 1(b)], with the thickness defined as:

$$t(x) = F_1(x) - F_2(x). \tag{3}$$

Similarly, after normalizing the corneal thickness, the thickness heterogeneity (TH) was defined as the variance of the thickness [Fig. 1(b)]:

$$TH = \mathrm{var}(t). \tag{4}$$

2.3. Micro variable calculation method

To quantitatively assess the morphological characteristics of fibrous structures, we have previously proposed a weighted vector summation algorithm [24], which can detect the orientation of fiber-like structures in a pixel-wise manner (Supplement 1, Fig. S4). Based on this, for 2D OCT images of the cornea, it was sufficient to have an azimuthal angle θ to define the direction of collagen fibers [Fig. 1(c)]. Then 2D directional variance DV_{2D} was calculated by the following equation:

$$DV_{2D} = 1 - (C_{2D}^2 + S_{2D}^2)^{1/2}, \tag{5}$$

where $C_{2D} = \sum_{j=1}^{n} \cos(2\theta_j)$, $S_{2D} = \sum_{j=1}^{n} \sin(2\theta_j)$, n is the number of fiber pixels in the region, and θ_j is the calculated orientation. Directional variance (DV) was proposed to quantify the level of fiber alignment [Fig. 1(d)] [25,26]. DV ranged between 0 and 1, with larger values representing a more disordered arrangement of fibrous structures (Supplement 1, Fig. S5). We set the size of the local area (*i.e.*, the window size for DV calculation) as 7×7 pixels for all the samples in this study, corresponding to an actual size of 55×55 μm.

2.4. Co-registered OCT/SHG imaging of human corneas

The corneal tissue is thought to be full of collagen fibers [27], and second-harmonic generation (SHG) microscopy, a molecule-specific modality, is regarded as the gold standard for collagen fiber imaging [28]. To explore the contrast on corneal images acquired by OCT, a co-registered OCT/SHG imaging was performed. Human cornea samples were obtained from clinical donations, and the same cornea piece was imaged by a custom spectral-domain OCT system (Supplement 1, Fig. S6) and a commercial SHG system (Stellaris 8 DIVE, Leica, Germany) separately. Briefly, a dual cascade super-luminescent diode (SLD, SUPERLUM, Ireland) was selected as the light source of the OCT system, with a center wavelength of 840 nm and a spectral bandwidth of 47 nm. The A-scan acquisition rate used in this experiment was 100 kHz, with a pixel count of 2048. For SHG imaging, a femtosecond mode-locked Ti:Sapphire laser (140 fs, 80 MHz) tunable in the range of 680-1300 nm was used as the light source. The system captured SHG signals

Biomedical Optics EXPRESS

from collagen fibers of corneas at 400 ± 10 nm at 800 nm excitation, utilizing a Plan-Apochromat 25× water-immersion objective (NA = 0.95, Leica, Germany). The system provided a field of view of 0.46×0.46 mm^2 with approximately 0.9 μm spatial resolution.

2.5. Parameter importance assessment

While our calculations highlighted macro and micro structural alterations with keratoconus progression, the independence of the three variables complicated clinical evaluation. To streamline diagnosis and establish a quantitative clinical criterion, it was necessary to integrate three variables into one unified parameter, which required determining their relative importance in keratoconus assessment to assign appropriate weights. Random Forest (RF), an ensemble learning method, enhanced classification performance by aggregating predictions from multiple decision trees [29]. Each tree was trained on a bootstrapped subset of data with random feature selection during splitting, reducing overfitting through majority voting. Crucially, since RF randomly selected feature splits during tree growth, the algorithm quantified feature importance by evaluating variable contributions to classification accuracy [30]. The 104 samples were standardized and partitioned into training (62 samples: 31 keratoconus, 31 normal) and test sets (42 samples: 20 keratoconus, 22 normal). Using the training set only, the optimal parameters of the RF model were determined by the grid search method (Supplement 1, Fig. S7), and the importance of each variable was obtained.

2.6. Determination of classification threshold

In binary classification, Support Vector Machines (SVM) inherently generated a decision function as:

$$\mathrm{D}(x) = \mathrm{w}^T \phi(x) + c, \tag{6}$$

where w^T is the weight vector, $\phi(x)$ denotes a kernel-induced feature mapping, and c is the bias term. The default decision threshold for classifying samples was $\mathrm{D}(x) = 0$, which was applicable to balanced samples with no specific cost preferences. However, in practical applications, especially in clinical diagnosis scenarios where misclassification led to significant costs, adjusting the decision threshold was critical to optimize performance metrics such as precision or recall. The receiver operating characteristic (ROC) curve showed the true positive rate (TPR) against the false positive rate (FPR) at different thresholds. The optimal threshold can be selected by maximizing the Youden index (J):

$$J = TPR - FPR. \tag{7}$$

The threshold corresponding to the maximum value of the Youden index represented the optimal solution that theoretically balanced sensitivity and specificity. Based solely on the distribution of the data, J was the point on the ROC curve closest to the upper-left corner (the point of perfect classification). Based on this, the point with a false negative rate not exceeding 5% and closest to the maximum Youden index was selected as the final threshold point.

2.7. Statistical analysis

To evaluate the existence of significant differences among different groups, we used a two-tailed t-test, and results were considered significant at $P < 0.05$. Canonical linear discriminant analysis was performed using SPSS software (version 19.0, IBM Inc) to obtain original classification accuracy (OCA) and cross-validated classification accuracy (CVCA).

Biomedical Optics EXPRESS

3. Results

3.1. Verifying the origin of fiber-like structures in OCT images

Histological studies indicated that the corneal stroma constituted primarily of collagen fibers by weight [31,32]. Due to its high refractive index and fibrous nature, collagen fibers served as the primary scattering source in the stroma [33].Therefore, we hypothesized that the fiber-like structures observed in OCT images predominantly originated from collagen organization, and performed co-registered OCT/SHG imaging of human corneal tissues to confirm this, since SHG was assumed as a specific imaging modality for collagen fibers. Corneal areas with marked scars were imaged [Fig. 2(a), yellow trapezoidal box]. The OCT volume comprised 230 layers, while the SHG volume comprised 60 layers [Fig. 2(b)]. 3D reconstructions revealed strong spatial correspondence between OCT and SHG datasets [Fig. 2(c)].

For analysis and comparison, 2D cross-sectional images at identical depths were extracted from OCT and SHG volumes. Speckle noise and the intensity fluctuation brought by axial sensitivity decay, optical attenuation, and transverse luminance inhomogeneity degraded the quality of OCT images [Fig. 2(d)]. To address this issue, the Gaussian and homomorphic filtering were used to emphasize the high-frequency components and improve uniformity of local intensity, and adaptive thresholding and intensity remapping optimized the dynamic range of the images [Fig. 2(e)]. As a result, a higher similarity to SHG counterparts was achieved [Fig. 2(f)], which enabled the regional registration and collagen microstructure analysis from OCT data.

Further, 12 regions of interest (ROIs) were selected randomly within SHG fields, and for each ROI the DV metric was calculated which reflected the alignment level of collagen fibers. These 12 regions were divided into two categories according to DV values, denoted as Class 1 and 2, respectively, and then the same calculation was performed on the OCT images [Fig. 2(g), marked with blue and yellow boxes]. Although the absolute DV values were different, the significant disparity in DV between Class 1 and 2 observed in SHG data persisted in OCT-derived results [Fig. 2(h)]. Furthermore, correlation analysis demonstrated strong agreement between OCT and SHG measurements [Fig. 2(i)], confirming the feasibility of extracting micro organization of collagen fibers from clinical OCT images.

3.2. Multi-parametric analysis results

In vivo imaging was performed in the hospital using a commercial OCT system to acquire images from 104 clinical human corneal samples, including 51 keratoconus cases and 53 normal cases [Fig. 3(a)]. In particular, epidemiological studies indicated a male-to-female ratio of 0.9–2.5 : 1 for keratoconus in Asian populations, with male patients exhibiting earlier onset and faster disease progression [34]. Consequently, the proportion of male patients was higher than female in the keratoconus cohort provided by the hospital.

Using the method mentioned above, three parameters were calculated for all datasets: curvature heterogeneity (CH), thickness heterogeneity (TH), and directional variance (DV) of collagen fibers. Each parameter provided independent and complementary insights, as revealed by the correlation coefficient r marked in each graph [Fig. 3(c)]. The original classification accuracy (OCA) and cross-validated classification accuracy (CVCA) for identifying keratoconus cases from normal ones exceeded 90% when combining all three parameters together [Fig. 3(b)], while OCA and CVCA decreased when only two parameters were considered [Fig. 3(c)], highlighting the necessity of multi-parametric analysis from different perspectives. More impressively, the classification accuracy with the inclusion of the microscopic feature (*i.e.*, DV) was higher than that with macroscopic parameters (*i.e.*, TH and CH) only, which indicated that DV played an important role in identifying and understanding keratoconus. Our analysis results revealed that keratoconus cases exhibited markedly higher CH and TH at the macrostructural level, and significantly elevated DV at the microstructural level which reflected progressive disorganization of collagen fibers

Biomedical Optics EXPRESS

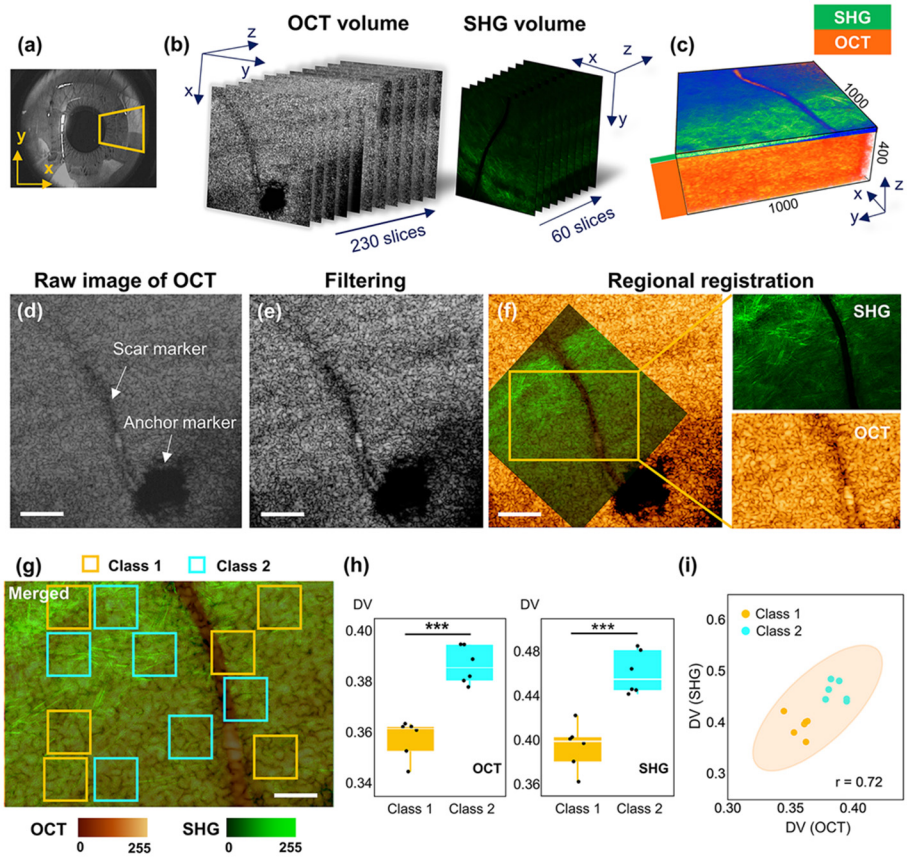

Fig. 2. Verifying the origin of fiber-like structures in OCT volumes. (a) The sampling method on human cornea samples (yellow trapezoidal box). (b) 3D scanning of corneal samples to obtain OCT volumes and SHG volumes, respectively. (c) Merged 3D volume maps of OCT and SHG for the same corneal region. (d) The original image (the 50th layer) acquired from OCT. The specific scar and anchor markers are pointed by white arrows. Scale bar, 600 μm. (e) Preprocessing of OCT images via Gaussian and homomorphic filtering, and intensity re-mapping. Scale bar, 600 μm. (f) Matching the SHG image to the OCT image according to the feature markers. The fiber-like structures in the representative ROI are zoomed in. Scale bar, 600 μm. (g) Twelve ROIs with the same physical dimensions were selected on the merged image to obtain DV from either image. Class 1 and Class 2 were categorized based on the average DV within each ROI. Scale bar, 250 μm. (h) Significant differences in DV between Class 1 and Class 2 in the SHG image were retained in analysis results from the OCT image. ***, $P < 0.001$. (i) A high correlation in DV from OCT and SHG images was obtained.

[Fig. 3(d)]. These findings suggested that during corneal deformation, the corneal curvature and thickness distribution changed dramatically as observed clinically, while the structural disruption of collagen fibers in stroma, typically ignored, likely stemmed from stress-induced fracturing of the lamellar collagen architecture during corneal deformation [Fig. 3(e)].

3.3. *Importance ranking of different variables*

To streamline diagnosis and establish a quantitative clinical criterion, we would like to integrate three variables into one unified parameter. Therefore, in this study we used Random Forest (RF)

Biomedical Optics EXPRESS

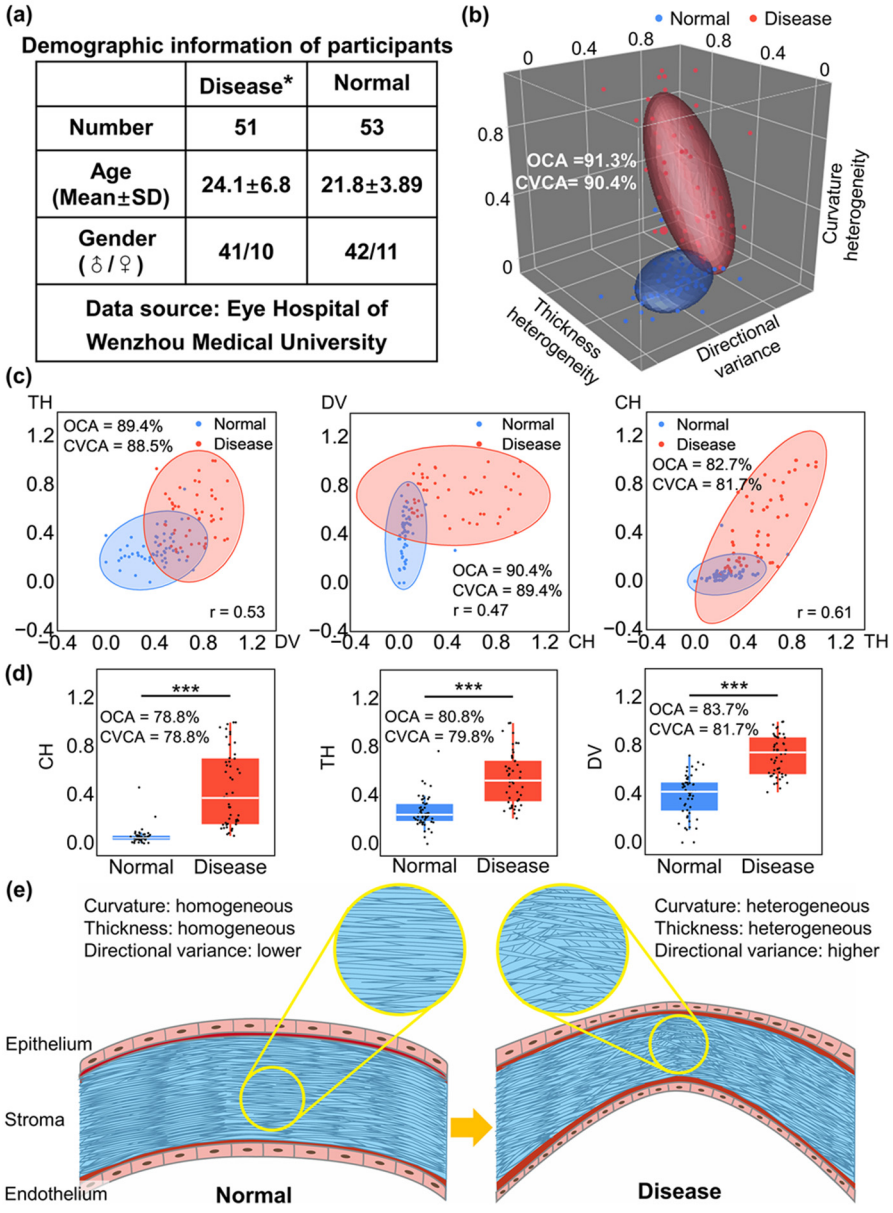

Fig. 3. Analysis results of human corneas by quantitative OCT imaging. (a) Demographic information of collected data. *, 46 out of 51 samples had the time of keratoconus diagnosis less than two years. (b) 3D scatterplot generated from a combination of all the three parameters. (c) 2D scatterplots generated from any two of the three parameters in distinguishing keratoconus samples from normal ones. Correlation coefficients (marked in the graph) satisfy the inequation: $|r| < 0.7$, indicating no offending parameters and independence among these three ones. OCA and CVCA values were labeled in each graph. (d) Boxplots of each parameter. $n = 51$ keratoconus samples, and $n = 53$ normal samples. ***, $P < 0.001$. OCA and CVCA values are labeled in each graph. (e) Schematic illustration of macro-micro structural changes in keratoconus.

Biomedical Optics EXPRESS

to determine relative importance of these variables to assign appropriate weights. Although error curves stabilized at 40 trees when misclassification rate of RF reached a low level and remained stable, the number of trees was set at 100 reasonably to ensure robustness, as tree numbers minimally impacted performance [Fig. 4(a)]. Leave-one-out cross-validation (LOOCV) was employed to mitigate overfitting risks in this limited dataset. For each iteration, 62 (out of 104) samples trained the model, and the remaining sample generated a prediction probability. The resulting receiver operating characteristic (ROC) curve yielded an area under the curve (AUC) of 0.969 [Fig. 4(b)], confirming strong discriminative power without overfitting.

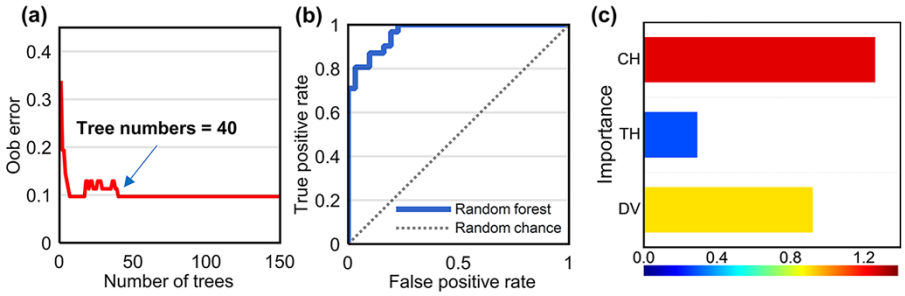

Fig. 4. Assessing parameter importance using the Random Forest (RF) model. (a) Error curve of the RF model. The error stabilized at 0.1 when the number of training trees reached 40. (b) ROC curve of the RF model, with an AUC of 0.969. (c) Importance assessment of the three parameters output by the RF model.

In this way, the importance rankings were successfully classified by RF using the 62 training set data [Fig. 4(c)]. Feature importance analysis ranked CH as the most critical metric, followed by DV and TH. Although the weight of TH was lower than CH and DV, the above-mentioned classification results (Fig. 3) demonstrated that TH exerted a positive effect in improving the classification accuracy in contrast to the usage of CH and DV only. Given the critical role of thickness variables in traditional keratoconus diagnostic measures, as well as the possibility of evaluation deviation due to limited datasets in this study, the TH parameter was retained for the following integration since it might hold potential for more comprehensive datasets. The output importance was normalized to serve as the weights of the three parameters, and further used to synthesize the final unified parameter, enabling a simplified yet comprehensive diagnostic framework.

3.4. KPI establishment and diagnostic performance

The discovery of stromal collagen alignment disordering during keratoconus progression offered critical insights, yet multi-parametric assessments might be impractical and inconvenient for clinical diagnosis. Following the acquisition of variable importance, the three parameters was synthesized into a unified quantitative parameter, keratoconus potential index (KPI), defined as a weighted combination of DV, CH and TH. This index integrated macro-micro structural information while leveraging optimized weights to maximize sensitivity.

In detail, for each corneal OCT image, heterogeneity in curvature and thickness (*i.e.*, CH and TH)—representing macroscopic structural changes—were multiplied by their respective weights and mapped across all pixels of corneal region as baseline indicators. Concurrently, pixel-wise DV, reflecting microscopic collagen disorganization, were weighted and superimposed [Fig. 5(a), left]. The weighted summation of these variables generated a pixel-wise KPI matrix, which was color-encoded and overlaid onto the corneal morphology. The pixel-wise features of KPI maps were derived from the pixel-wise information of DV maps, with representative paired DV and KPI maps shown in Supplement 1, Fig. S8. Warmer colors indicated higher

Biomedical Optics EXPRESS

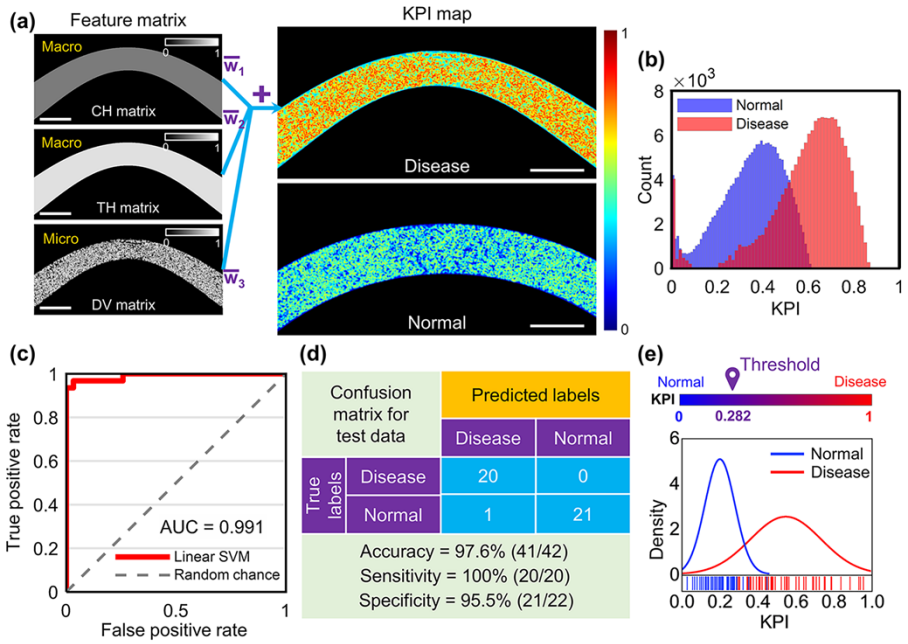

Fig. 5. KPI establishment and its application in keratoconus diagnosis. (a) The schematic showing the generation of the KPI metric by adding up the three weighted parameters. The right maps exhibited representative KPI maps for keratoconus and normal cornea samples. Scale bar, 1.5 mm. (b) Distributions of KPI for keratoconus and normal cornea. (c) ROC in the classification of normal and keratoconus samples using KPI. (d) Classification results for the 42 test dataset (20 keratoconus, 22 normal corneas). (e) Classification threshold and KPI distributions using the complete 104 samples.

KPI values and elevated keratoconus risk, whereas cooler colors denoted normative regions [Fig. 5(a), right]. These red areas reflected locations of disorganized collagen fibers, which might represent potential lesion areas of keratoconus. Distribution histograms revealed a distinct rightward shift in KPI for keratoconus [Fig. 5(b)]. A linear support vector machine (SVM) model was trained on KPI extracted from 62 training set (31 normal, 31 keratoconus) and evaluated by LOOCV. The ROC curve, with an AUC of 0.991 [Fig. 5(c)] comparable to or even better than multi-parametric analysis results [Fig. 4(b)], highlighted exceptional diagnostic capability from KPI-based assessments. When applied to the independent 42 test set (22 normal, 20 keratoconus), the model achieved 97.6% accuracy [100% sensitivity, 95.5% specificity, Fig. 5(d)]. Using the same method for training the KPI model, we have trained another SVM model using CH and TH respectively, also extracted from 62 training set (31 normal, 31 keratoconus) and evaluated by LOOCV (Supplement 1, Fig. S9). When applied to the independent 42 test set (22 normal, 20 keratoconus), the CH model achieved 83.3% accuracy (65% sensitivity, 100% specificity), and the TH model achieved 85.7% accuracy (85.0% sensitivity, 85.3% specificity). Therefore, the fused parameter KPI achieved improvement in accuracy (97.6%) compared to that from conventional macro-parameters only. To refine generalizability, the full dataset including 104 samples (53 normal, 51 keratoconus) was used to retrain the SVM, establishing a decision threshold valued at 0.282 which classified KPI-positive samples as high-risk and KPI-negative ones as normal [Fig. 5(e)].

Biomedical Optics EXPRESS

4. Discussion and conclusion

Keratoconus predominantly manifests during adolescence, with rising global incidence rates severely impacting patients' quality of life, occupational choices, and posing risks of blindness [3]. Current clinical diagnosis lacks standardized protocols, relying heavily on macroscopic corneal deformation metrics and subjective clinician expertise. Invasive biopsies or contact-based measurements are unsuitable for corneal evaluation due to ocular sensitivity [35]. Confocal microscopy, which provides exceptional resolution, allows for assessment of collagen lamellae orientation and identification of subtle disorganizations in the stromal architecture and keratocytes. However, confocal microscopy is limited by relatively small imaging areas and depth penetration, probably making it less suitable for comprehensive assessment of full cornea in a single examination [36]. Transmission interference microscopy (TIM) offers label-free quantitative imaging capabilities based on phase shifts rather than intensity variations, which provides great sensitivity to tiny variations (such as microscopic striae which are the precursors of keratoconus), potentially offering biomarkers for early detection of keratoconus progression [37], although further clinical validation is needed. While corneal topography via Penta-cam remains the main standard, its accuracy might be influenced by tear film variability, dark-room requirements, and the absence of quantitative thresholds, which necessitate the extensive clinical experience [9]. In contrast, OCT, advantaged with non-contact, high-resolution performance and rapid calculation, has emerged as a transformative tool in ophthalmic imaging. Full-field (FF)-OCT imaging of keratoconus has revealed characteristic alterations of collagen organization in the anterior cornea as well, yet at the cost of limited imaging depth and time efficiency [38,39]. Spectral-domain (SD)-OCT provides an excellent balance between imaging depth, resolution, and acquisition speed, making it well-suited for ophthalmic clinical applications owing to the capability of identifying microstructural alterations in cornea and limbus [40].

While SD-OCT allows for reconstruction of corneal microarchitecture, a precise quantitative characterization of microstructure is essential for detecting and diagnosing keratoconus. Against this backdrop, we develop a dual-scale diagnostic framework combining macrostructural (curvature, thickness of cornea) and microstructural (collagen fiber organization) features from clinical OCT images. Our analysis confirms marked increases in curvature and thickness heterogeneity during corneal ectasia, consistent with prior macrostructural studies [19]. Notably, we identify progressive disorganization of stromal collagen clusters, likely driven by biomechanical stress-induced cross-link disruption [22], which destabilizes lamellar architecture and accelerates central thinning. The development of collagen cross-link breaks may associate with a decrease in the bio-structural stability of the stromal layer in the cornea [41], which may also represent one of the internal causes of the overall keratoconus conization. Based on this, DV has been proved to perform a special and positive role in understanding collagen remodeling and degradation from keratoconus. The classification that incorporates the microscopic parameter DV provides improved precision and interpretation. These insights underpin KPI, a unified metric integrating weighted macro-micro structural parameters to quantify keratoconus risk with >95% sensitivity and specificity, which may address key limitations of subjective topography-dependent methods, offering a promising pathway for detection of keratoconus.

It is interesting to note that the ranking of the three parameters from classification accuracy values [shown in Fig. 3(d)] and Random Forest (RF) analysis [shown in Fig. 4(c)] is different. On the one hand, the number of patients used for analysis was different [*i.e.*, 104 data points for Fig. 3(d), and 62 data points for Fig. 4(c)] since we separated the overall data pool into the training set (used for RF analysis in Fig. 4) and the test set (used for assessing the performance of KPI, as shown in Fig. 5). On the other hand, the mechanism used for evaluating the importance of each parameter in these two cases was different. Specifically, the calculation of OCA and CVCA was based on the data of each parameter individually, while the importance ranking from the RF analysis was obtained considering mutual interactions of these parameters. Moreover, as

Biomedical Optics EXPRESS

a preliminary study, currently the data applied to the RF analysis were limited, and more data would be collected in our future work to improve and stabilize the weight for the construction of the fused parameter KPI.

Clinically, KPI leverages OCT's widespread availability, non-invasiveness, and rapid imaging capabilities, making it ideal for screening and postoperative monitoring. By providing an objective threshold and pixel-wise risk maps, KPI reduces reliance on clinician experience and enables quantitative tracking of treatment outcomes. While a common weakness of OCT imaging is lacking molecular specificity, previous studies have revealed that polarization-sensitive OCT can enhance collagen characterization under specific conditions by exploiting its birefringent properties of collagen fibers [42,43]. While OCT may not be able to distinguish submicron-scale collagen fibers or nano-scale fibrils, it may detect scattering signals from fiber clusters, at the micrometer scale. Although it is difficult to obtain molecular information, we have demonstrated that it is feasible for OCT to extract the spatial distribution characteristics from the scattering signals of fiber-like microstructures [44]. The information that we studied does not actually pertain to the structure of the individual collagen fiber, but rather to the layered structural arrangement resulting from collagen cross-linking or stacking. Besides, keratocytes, which are generally distributed between the lamellae of collagen fibers [45], might also contribute to the obtained structural features by themselves and by inducing remodeling of collagen fibers. High-resolution OCT which offers improved lateral and axial resolutions may provide better-quality images for the calculation and analysis of scattering signals [40].In addition, spatial features such as fiber waviness may further refine collagen analysis [46], providing additional clues for studying microstructural changes. In clinical diagnosis, keratoconus patients often present to the clinic during advanced stages. Further study of collagen changes may yield earlier information about keratoconus, which will be highly beneficial for early warning. Longitudinal studies correlating collagen disorganization with disease onset can enable pre-symptomatic screening, with the promise of reducing the need for corneal transplantation. As a preliminary longitudinal analysis, we obtained KPI for keratoconus at different stages (Supplement 1, Fig. S10), highlighting the potential of this fused parameter in keratoconus staging. Expanding datasets will also refine KPI thresholds and weights, improving diagnostic robustness.

In summary, we identified potential changes in collagen fibers related to keratoconus based on clinical corneal OCT data, and developed a solution for keratoconus diagnosis incorporating both macroscopic and microscopic properties of the cornea. This approach not only delivered clinician-friendly visualizations but also provided a highly-sensitive quantitative evaluation index. With further technical improvements, our method may become a potentially non-invasive, high-sensitivity, and universal technique for keratoconus detection, leading to early recognition and timely treatment to reduce the risk of keratoconus.

Funding. National Natural Science Foundation of China (62275232, 62035011, 11974310, 31927801, 62375104); Natural Science Foundation of Zhejiang Province (LZ25F050007); National Administration of Traditional Chinese Medicine (NATCM); Zhejiang Joint TCM Science and Technology Program (GZY-ZJ-KJ-24089).

Acknowledgements. We thank Prof. Shean-Jen Chen from National Yang Ming Chiao Tung University for insightful discussion.

Disclosures. The authors declare that there are no conflicts of interest related to this article.

Data availability. The custom MATLAB code for multiparametric analysis, including Orientation and DV, has been deposited in GitHub [47]. The custom MATLAB code for the random forest algorithm and examples have been deposited in GitHub [48], as well. The data that support the findings of this study are available from the corresponding authors upon reasonable request.

Supplemental document. See Supplement 1 for supporting content.

Biomedical Optics EXPRESS

References

1. K. Zadnik, J. T. Barr, M. O. Gordon, *et al.*, "Biomicroscopic Signs and Disease Severity in Keratoconus," Cornea **15**(2), 139–146 (1996).
2. X. Li, Y. S. Rabinowitz, K. Rasheed, *et al.*, "Longitudinal study of the normal eyes in unilateral keratoconus patients," Ophthalmology **111**(3), 440–446 (2004).
3. V. Mas Tur, C. MacGregor, R. Jayaswal, *et al.*, "A review of keratoconus: Diagnosis, pathophysiology, and genetics," Surv. Ophthalmol. **62**(6), 770–783 (2017).
4. M. A. Henriquez, M. Hadid, and L. Izquierdo, "A Systematic Review of Subclinical Keratoconus and Forme Fruste Keratoconus," J. Refract. Surg. **36**(4), 270–279 (2020).
5. A. Martínez-Abad and D. P. Piñero, "New perspectives on the detection and progression of keratoconus," J. Cataract Refractive Surg. **43**(9), 1213–1227 (2017).
6. P. Kanclerz, R. Khoramnia, and X. Wang, "Current Developments in Corneal Topography and Tomography," Diagnostics **11**(8), 1466 (2021).
7. R. Vinciguerra, R. Ambrósio, A. Elsheikh, *et al.*, "Detection of Keratoconus With a New Biomechanical Index," J. Refract. Surg. **32**(12), 803–810 (2016).
8. N. Falgayrettes, E. Patoor, F. Cleymand, *et al.*, "Biomechanics of keratoconus: Two numerical studies," PLoS One **18**(2), e0278455 (2023).
9. R. Ambrósio, A. P. Machado, E. Leão, *et al.*, "Optimized Artificial Intelligence for Enhanced Ectasia Detection Using Scheimpflug-Based Corneal Tomography and Biomechanical Data," Am. J. Ophthalmol. **251**, 126–142 (2023).
10. R. Ambrósio, B. T. Lopes, F. Faria-Correia, *et al.*, "Integration of Scheimpflug-Based Corneal Tomography and Biomechanical Assessments for Enhancing Ectasia Detection," J. Refract. Surg. **33**(7), 434–443 (2017).
11. J. A. P. Gomes, D. Tan, C. J. Rapuano, *et al.*, "Global Consensus on Keratoconus and Ectatic Diseases," Cornea **34**(4), 359–369 (2015).
12. M. W. Belin, O. F. Villavicencio, and R. R. J. Ambrósio, "Tomographic Parameters for the Detection of Keratoconus: Suggestions for Screening and Treatment Parameters," Eye Contact Lens **40**(6), 326–330 (2014).
13. B. E. Bouma, J. F. de Boer, D. Huang, *et al.*, "Optical coherence tomography," Nat. Rev. Methods Primers **2**(1), 79 (2022).
14. M. Ang, M. Baskaran, R. M. Werkmeister, *et al.*, "Anterior segment optical coherence tomography," Prog. Retin. Eye Res. **66**, 132–156 (2018).
15. D. Z. Reinstein, M. Gobbe, T. J. Archer, *et al.*, "Epithelial, Stromal, and Total Corneal Thickness in Keratoconus: Three-dimensional Display With Artemis Very-high Frequency Digital Ultrasound," J. Refract. Surg. **26**(4), 259–271 (2010).
16. D. Z. Reinstein, T. J. Archer, and M. Gobbe, "Corneal Epithelial Thickness Profile in the Diagnosis of Keratoconus," J. Refract. Surg. **25**(7), 604–610 (2009).
17. J. Franco, C. A. White, and J. N. Kruh, "Analysis of Compensatory Corneal Epithelial Thickness Changes in Keratoconus Using Corneal Tomography," Cornea **39**(3), 298–302 (2020).
18. Y. Li, O. Tan, R. Brass, *et al.*, "Corneal Epithelial Thickness Mapping by Fourier-Domain Optical Coherence Tomography in Normal and Keratoconic Eyes," Ophthalmology **119**(12), 2425–2433 (2012).
19. Y. Li, W. Chamberlain, O. Tan, *et al.*, "Subclinical keratoconus detection by pattern analysis of corneal and epithelial thickness maps with optical coherence tomography," J. Cataract Refractive Surg. **42**(2), 284–295 (2016).
20. K. Y. Kim, S. Lee, Y. J. Jeon, *et al.*, "Anterior segment characteristics in normal and keratoconus eyes evaluated with a new type of swept-source optical coherence tomography," PLoS One **17**(9), e0274071 (2022).
21. D. A. Godefrooij, G. A. de Wit, C. S. Uiterwaal, *et al.*, "Age-specific Incidence and Prevalence of Keratoconus: A Nationwide Registration Study," Am. J. Ophthalmol. **175**, 169–172 (2017).
22. A. Alhayek and P. R. Lu, "Corneal collagen crosslinking in keratoconus and other eye disease," Int. J. Ophthalmol-Chi **8**(2), 407–418 (2015).
23. Z. Heidari, M. Mohammadpour, K. Amanzadeh, *et al.*, "Evaluation of corneal topographic, tomographic and biomechanical indices for detecting clinical and subclinical keratoconus: a comprehensive three-device study," Int. J. Ophthalmol. **14**(2), 228–239 (2021).
24. Z. Y. Liu, K. P. Quinn, L. Speroni, *et al.*, "Rapid three-dimensional quantification of voxel-wise collagen fiber orientation," Biomed. Opt. Express **6**(7), 2294–2310 (2015).
25. Z. Y. Liu, D. Pouli, D. Sood, *et al.*, "Automated quantification of three-dimensional organization of fiber-like structures in biological tissues," Biomaterials **116**, 34–47 (2017).
26. W. J. Liu, Y. S. Yao, J. Meng, *et al.*, "Architecture- driven quantitative nanoscopy maps cytoskeleton remodeling," Proc. Natl. Acad. Sci. U.S.A. **121**(42), 2410688121 (2024).
27. K. M. Meek and N. J. Fullwood, "Corneal and scleral collagens—a microscopist's perspective," Micron **32**(3), 261–272 (2001).
28. R. M. Williams, W. R. Zipfel, and W. W. Webb, "Interpreting Second-Harmonic Generation Images of Collagen I Fibrils," Biophys. J. **88**(2), 1377–1386 (2005).
29. J. L. Speiser, M. E. Miller, J. Tooze, *et al.*, "A comparison of random forest variable selection methods for classification prediction modeling," Expert Syst. Appl. **134**, 93–101 (2019).
30. P. Probst, M. N. Wright, and A.-L. Boulesteix, "Hyperparameters and tuning strategies for random forest," WIREs Data Min. Knowl. Discovery **9**(3), e1301 (2019).

Biomedical Optics EXPRESS

31. K. M. Meek and C. Knupp, "Corneal structure and transparency," Prog. Retin. Eye Res. **49**, 1–16 (2015).
32. K. M. Meek and C. Boote, "The organization of collagen in the corneal stroma," Exp. Eye Res. **78**(3), 503–512 (2004).
33. M. S. Sridhar, "Anatomy of cornea and ocular surface," Indian J. Ophthalmol. **66**(2), 190–194 (2018).
34. J. S. Saini, S. Vandana, P. Singh, *et al.*, "Keratoconus in Asian eyes at a tertiary eye care facility," Clin. Exp. Optom. **87**(2), 97–101 (2004).
35. J. Santodomingo-Rubido, G. Carracedo, A. Suzaki, *et al.*, "Keratoconus: An updated review," Contact Lens Anterior Eye **45**(3), 101559 (2022).
36. R. F. Guthoff, C. Baudouin, and J. Stave, *Atlas of Confocal Laser Scanning In-Vivo Microscopy in Ophthalmology*. (Springer, 2006), Chap. 5.
37. S. Alhaddad, W. Ghouali, C. Baudouin, *et al.*, "Transmission interference microscopy of anterior human eye," Nat. Commun. **16**(1), 7838 (2025).
38. V. Mazlin, P. Xiao, E. Dalimier, *et al.*, "In vivo high resolution human corneal imaging using full-field optical coherence tomography," Biomed. Opt. Express **9**(2), 557–568 (2018).
39. E. Auksorius, D. Borycki, P. Stremplewski, *et al.*, "In vivo imaging of the human cornea with high-speed and high-resolution Fourier-domain full-field optical coherence tomography," Biomed. Opt. Express **11**(5), 2849–2865 (2020).
40. L. Han, B. Tan, Z. Hosseinaee, *et al.*, "Line-scanning SD-OCT for in-vivo, non-contact, volumetric, cellular resolution imaging of the human cornea and limbus," Biomed. Opt. Express **13**(7), 4007–4020 (2022).
41. P. Maier, T. Reinhard, and M. Kohlhaas, "Corneal Collagen Cross-Linking in the Stabilization of Keratoconus," Dtsch Arztebl Int. **116**(11), 184–190 (2019).
42. S. K. Nadkarni, M. C. Pierce, B. H. Park, *et al.*, "Measurement of Collagen and Smooth Muscle Cell Content in Atherosclerotic Plaques Using Polarization-Sensitive Optical Coherence Tomography," Journal of the American College of Cardiology **49**(13), 1474–1481 (2007).
43. Z. Liu, J. Jia, Q. Lei, *et al.*, "Electrohydrodynamic Direct-Writing Micro/Nanofibrous Architectures: Principle, Materials, and Biomedical Applications," Adv. Healthcare Mater. **13**(28), 2400930 (2024).
44. T. Han, S. Qian, J. Meng, *et al.*, "Detection of Human Cervical Cancer by Probe-Based Quantitative Optical Coherence Tomography," Laser Photonics Rev. **19**(9), 2401479 (2025).
45. F. H. Silver, D. Benedetto, and T. Deshmukh, "Changes in Corneal Keratocytes and Collagen Fibrils as an Indicator of Keratoconus Onset: A Preliminary Study Based on OCT Subchannel Images," Front. Biosci. **30**(6), 38750 (2025).
46. S. Qian, J. Meng, Z. Feng, *et al.*, "Mapping Organizational Changes of Fiber-Like Structures in Disease Progression by Multiparametric, Quantitative Imaging," Laser Photonics Rev. **16**(6), 2100576 (2022).
47. C. Chen, "3D-Orientation-Variance-code," Github, 2025, https://github.com/LingxZhou/3D-Orientation-Variance-code.
48. C. Chen, "Random forest code," Github, 2025, https://github.com/ChangxChen/random-forest-code.